PHYSICAL REVIEW APPLIED **22,** 024023 (2024)

Wireless acoustic energy harvesting through an air-water metasurface with dual coupling resonators

Zhiwen Ren,[1] Hao-Wen Dong,[1,*] Sheng-Dong Zhao,[2] Mingji Chen,[1] and Daining Fang[1]

[1] *Institute of Advanced Structure Technology, Beijing Institute of Technology, Beijing 100081, China*
[2] *School of Mathematics and Statistics, Qingdao University, Qingdao 266071, China*

(Received 7 April 2024; revised 21 June 2024; accepted 12 July 2024; published 8 August 2024)

Extremely large acoustic impedance mismatching generates a natural acoustic barrier at the air-water interface, resulting in significantly impeding bidirectional acoustic wave propagation across the heterogeneous interface. Here, an air-water metasurface with dual coupling resonators is proposed to enhance the acoustic transmission at the air-water interface, which facilitates the implementation of wireless harvesting for acoustic energy across the heterogeneous interface. A theoretical model is established and derived to obtain the analytical expressions between acoustic energy transmission and microstructural geometric parameters. The theoretical analysis reveals that the highly efficient energy transmission mechanism depends on the impedance coupling effect of the resonant cavities for nonresonance modes. The enhanced bidirectional acoustic energy transmission at the air-water interface is investigated and verified numerically and experimentally, and the maximum enhancement of energy transmission is measured to be approximately 19 dB at the peak frequency. Finally, wireless acoustic energy harvesting across the air-water interface is implemented experimentally by integrating the designed metasurface with a contact-separation-mode triboelectric nanogenerator, and the captured energy from the waves effectively operates six LED lamps. The proposed "bottom-up" design methodology of air-water wave energy harvesting based on an acoustic-metasurface-embedded system opens promising routes for underwater wireless energy-supplying platforms and medical ultrasound therapy.

DOI: 10.1103/PhysRevApplied.22.024023

I. INTRODUCTION

When acoustic waves propagate forward from one background medium to another, energy transmission at heterogeneous interfaces depends on the acoustic impedance difference between the mediums [1,2]. Extremely large acoustic impedance mismatching with a ratio of 3600 between the water and air implies only 0.1% of the incident acoustic energy is allowed to transmit through the air-water interface. These nearly perfect acoustic barrier boundaries, with a transmission loss of 30 dB, greatly hinder the cross-media interactivity of acoustic information and energy. Thus, enhancing air-water wave transmission efficiency shows promising applications for acoustic imaging [3–5], detection and sensing [6–9], remote communication [10,11], etc.

Recently, discarding a commonly-used quarter-wavelength impedance-matching approach, acoustic metamaterials and metasurfaces [1,12–21] are applied to break the acoustic barrier at the air-water interface, e.g., the usage of evanescent waves [22,23], membrane type structure [24], coupling-bubbles type structure [25–29], and gradient impedance type structure [30]. Low-frequency evanescent waves have been theoretically investigated for transmitting acoustic energy only close to the interface [22,23], which is not conducive to energy capture in the far field. For metamaterials with membranes, energy transmission can be greatly enhanced by constructing flexible components and induced local resonance modes [25], although it still requires improving mechanical stiffness in practical systems. For the bubbled-based metasurfaces, the bubble units, equivalent to flexible springs near the air-water heterogeneous interface [25,26], are constructed by using the hydrophobic characteristics of the microstructure surface [27–29], although they face the challenge of the bubbles' stability and complex hydrophobic treatment. A gradient impedance design has been proposed to broaden the transmission band at the air-water interface that further realizes cross-media acoustic communication [30,31]. In addition, the acoustic metasurfaces with designed transmission phase distributions can generate cross-media focusing beams and vortex beams with orbital angular momentum [32,33]. Previous studies have made numerous contributions to overcoming impedance mismatching at the interface through various transmission-enhanced metamaterials and metasurfaces. They have further realized

---

[*] Contact author: hwdong@bit.edu.cn

several fascinating water-air functionalities, e.g., acoustic communication [30], acoustic imaging [29], music transmission [28], and remote eavesdropping [32]. However, the functionality of wireless and remote acoustic energy harvesting [34] across the air-water interface has not yet been achieved systematically, which has potential applications in the cross-media energy supply for underwater electronic equipment.

In this work, an air-water metasurface with dual coupling resonators, which has a different microstructural topology from the previous works [22–33], is proposed to enhance the acoustic energy transmission at the air-water interface and then implement wireless acoustic wave energy harvesting. Acoustic wave propagation through the metasurface is described by a theoretical model. The theoretical design principles and physical mechanisms are revealed for highly efficient transmission. Then, the wave capacities of enhancing bidirectional acoustic energy transmission are shown and verified numerically and experimentally. Finally, remote wireless cross-media acoustic energy harvesting is realized by integrating a contact-separation-mode triboelectric nanogenerator (TENG) and the designed passive metasurface.

This paper is organized as follows. Sec. II presents a microstructure topology of the air-water metasurface and its transmission enhancement behavior of acoustic energy at the air-water interface is analyzed theoretically. Subsequently, acoustic energy transmission across the air-water interface is investigated and verified by numerical simulations and experiments in Sec. III. Finally, Sec. IV realizes wireless acoustic energy harvesting across the air-water interface via the metasurface and the TENG.

II. AIR-WATER METASURFACE WITH DUAL COUPLING RESONATORS

A. Configuration design of metasurface

To enhance energy transmission at the air-water interface, an acoustic metasurface with dual coupling resonators is proposed, as depicted in Fig. 1. Different from a bare air-water surface, a well-designed passive metasurface can help acoustic energy incident from the air domain to transmit efficiently into the water, see Fig. 1(a), and then the energy is harvested and converted by underwater transducers to the charge energy-storage device. Similarly, underwater acoustic energy can drive the electronic device to operate in the air domain via the passive metasurface. The microstructure of the acoustic metasurface consists of a long channel (region II), two parallel Helmholtz resonators (region IV), and connected coupling apertures (region III), as shown in Fig. 1(b). The channel's length is $l_1 + l_2$ and the width is h_{unit}; the resonator's length is $l_{c1} + l_{c2}$ and the width is h_c and the coupling aperture's length is l_n and the width is h_n. Given a geometric constraint of $l_1 - l_{c1} = l_2 - l_{c2}$ for analyzing the wave mechanisms more succinctly, the microstructural symmetry regarding the y-axis can be varied by adjusting the aperture position. Moreover, $l_1 = l_2$ denotes the symmetric configuration, while $l_1 \neq l_2$ signifies the asymmetric configuration.

B. Establishment of sound propagation model

Periodically arranged microstructures are placed at the air-water interface, as shown in Figs. 1(b) and 1(c), and the internal channels within the microstructure are filled with air. To elucidate the acoustic propagation characteristics within the proposed metasurface, a theoretical model is established with general acoustic pressure and particle velocity fields [28,29,35,36], while the structure walls are regarded as acoustic hard-wall boundaries. According to grating theory [37–40], when a plane wave is normally incident from region I, the acoustic pressure fields $p(x,y)$ and the velocity fields $v_x(x,y)$ in the medium for regions I and V should be rigorously expressed as follows [38,40]:

$$p(x,y) = \sum_{n=0}^{\pm\infty} e^{-iG_n y}(P_{I-n}e^{-i\beta_n x} + P_{R-n}e^{i\beta_n x}), \tag{1}$$

$$v_x(x,y) = \sum_{n=0}^{\pm\infty} \frac{\beta_n}{\rho\omega} e^{-iG_n y}(P_{I-n}e^{-i\beta_n x} - P_{R-n}e^{i\beta_n x}), \tag{2}$$

where ρ and ω are the mass density of the medium and the angular frequency of the wave, respectively; P_{I-n} and P_{R-n} are the complex amplitudes of the nth-order incident and reflective wave, respectively. Obviously, in region I, $P_{I-n} = 0$ for $n = \pm 1, \pm 2, \ldots \pm\infty$ and, in region V, $P_{R-n} = 0$ for $n = 0, \pm 1, \pm 2, \ldots, \pm\infty$. The term $G_n = 2n\pi/h_{\text{unit}}$ denotes the nth reciprocal lattice vector and it can be used to determine the wave number along the x-direction of the nth mode wave. When the microstructure constant, h_{unit}, is small compared with the working wavelength, the diffraction modes in regions I and V will not occur. In this work, the transmission behavior in the low-frequency band of the proposed metasurface is mainly examined. Thus, Eqs. (1) and (2) at $x = x_0$ can be simplified as follows:

$$\begin{bmatrix} p \\ v \end{bmatrix} = \begin{bmatrix} P_I & P_R \\ v_I & -v_R \end{bmatrix} \begin{bmatrix} e^{-ikx_0} \\ e^{ikx_0} \end{bmatrix}, \tag{3}$$

where P_I and P_R are the complex amplitudes of pressure for the incident and reflected waves, respectively. v_I and v_R are the complex amplitudes of velocity, respectively. Furthermore, $k = 2\pi f/c$ is the wave number of sound traveling in the medium with a sound velocity c at a frequency f. According to the acoustic impendence $Z = p/v$, the volume velocity of the channel section S is determined as $vS = pY$ after introducing surface acoustic admittance $Y = S/Z$. The effect of viscous and thermal losses is neglected in the channels.

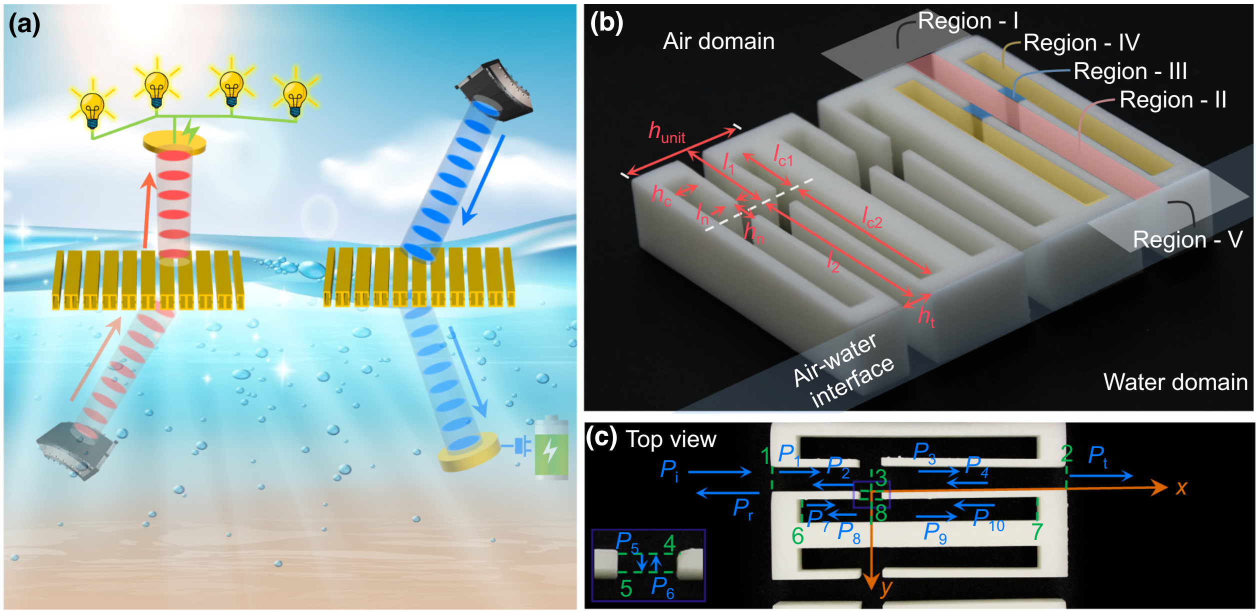

FIG. 1. Wireless acoustic energy harvesting via air-water metasurface. (a) Function demonstration of wireless acoustic energy harvesting across air-water interface via passive metasurface. (b) Photograph of the proposed metasurface with dual coupling resonators, which are manufactured via 3D printing technology, and it is shown as an example of the three-arranged microstructures. (c) Top view of the proposed metasurface.

When acoustic waves are incident from region I, the continuity principle of the acoustic pressure and volume velocity at cross-section 1 ($x = -l_1$) derives the following expression:

$$\begin{bmatrix} 1 & 1 \\ Y_0 & -Y_0 \end{bmatrix} \begin{bmatrix} P_i \\ P_r \end{bmatrix} = \begin{bmatrix} 1 & 1 \\ Y_t & -Y_t \end{bmatrix} \begin{bmatrix} P_1 e^{ik_t l_1} \\ P_2 e^{-ik_t l_1} \end{bmatrix}, \tag{4}$$

where P_i and P_r are the complex amplitudes of the acoustic pressure for the incident and reflected waves in region I, respectively. Moreover, P_1 and P_2 are the complex amplitudes of the pressure for the incident and reflected waves in region II, respectively; $Y_0 = h_{\text{unit}}/Z_i = h_{\text{unit}}/\rho_i c_i$ and $Y_t = h_t/Z_t = h_t/\rho_t c_t$ are the surface acoustic admittance for regions I and II, respectively, at cross-section 1.

The acoustic pressure and volume velocity fields at cross-section 2 satisfy the following:

$$\begin{bmatrix} 1 & 1 \\ Y_t & -Y_t \end{bmatrix} \begin{bmatrix} P_1 \\ P_2 \end{bmatrix} = \begin{bmatrix} \xi & \xi \\ Y_t & -Y_t \end{bmatrix} \begin{bmatrix} P_3 \\ P_4 \end{bmatrix} + \begin{bmatrix} 1-\xi & 1-\xi \\ 2Y_n & -2Y_n \end{bmatrix} \begin{bmatrix} P_5 \\ P_6 \end{bmatrix}, \tag{5}$$

where $Y_n = h_n/Z_n = h_n/\rho_n c_n$ denotes the surface acoustic admittance of region III at cross-section 3, and the constant term ξ is 1 or 0. Similarly, abiding by the continuity principle at cross-section 2 leads to the following equation:

$$\begin{bmatrix} 1 & 1 \\ Y_t & -Y_t \end{bmatrix} \begin{bmatrix} P_3 e^{-ik_t l_2} \\ P_4 e^{ik_t l_2} \end{bmatrix} = \begin{bmatrix} 1 & 1 \\ Y_{\text{trans}} & -Y_{\text{trans}} \end{bmatrix} \begin{bmatrix} P_t \\ 0 \end{bmatrix}, \tag{6}$$

where P_t denotes the transmitted waves in region V with the surface acoustic admittance $Y_{\text{trans}} = h_{\text{unit}}/Z_{\text{trans}} = h_{\text{unit}}/\rho_{\text{trans}} c_{\text{trans}}$ at cross-section 2. After introducing four terms, i.e., $A = Y_0 - Y_t/Y_0$, $B = Y_0 + Y_t/Y_0$, $C = Y_t - Y_{\text{trans}}/Y_t$, and $D = Y_t + Y_{\text{trans}}/Y_t$, solutions to Eq. (6) are derived as:

$$P_3 = \frac{P_t D}{2} e^{ik_t l_2},$$
$$P_4 = \frac{P_t C}{2} e^{-ik_t l_2}, \tag{7}$$

Then, Eq. (4) can lead to

$$2P_i = P_1 B e^{ik_t l_1} + P_2 A e^{-ik_t l_1}. \tag{8}$$

Combining Eq. (7), Eq. (8), and $P_1 = P_3 + P_4 - P_2$ obtained from Eq. (5) leads to

$$P_2 = \frac{2P_i - P_t(De^{ik_t l_2} + Ce^{-ik_t l_2})Be^{ik_t l_1}}{2Ae^{-ik_t l_1} - 2Be^{ik_t l_1}}. \tag{9}$$

When acoustic waves propagate in the bilateral resonant cavities, volume velocities at cross-sections 6 and 7 have rigid boundaries equal to zero, namely

$$(P_7 e^{-ik_c(-l_{c1})} - P_8 e^{ik_c(-l_{c1})}) Y_c = 0 \ ,$$
$$(P_9 e^{-ik_c l_{c2}} - P_{10} e^{ik_c l_{c2}}) Y_c = 0 \ . \tag{10}$$

Similarly, when acoustic waves propagate through cross-section 5, the continuity principle indicates

$$\begin{bmatrix} 1 & 1 \\ Y_n & -Y_n \end{bmatrix} \begin{bmatrix} P_5 e^{-ik_n l_n} \\ P_6 e^{ik_n l_n} \end{bmatrix} = \begin{bmatrix} \xi & \xi \\ -Y_c & Y_c \end{bmatrix} \begin{bmatrix} P_7 \\ P_8 \end{bmatrix} + \begin{bmatrix} 1-\xi & 1-\xi \\ Y_c & -Y_c \end{bmatrix} \begin{bmatrix} P_9 \\ P_{10} \end{bmatrix}, \tag{11}$$

Hence, the acoustic impedance of cross-section 5 is determined as

$$Z_c = \frac{P_5 e^{-ik_n l_n} + P_6 e^{ik_n l_n}}{(P_5 e^{-ik_n l_n} - P_6 e^{ik_n l_n}) Y_n} = \frac{P_7 + P_8}{(-P_7 + P_8) Y_c + (P_9 - P_{10}) Y_c}. \tag{12}$$

Here, inserting Eq. (10) into Eq. (12) leads to

$$Z_c = -\frac{i}{Y_c} \frac{\cos(k_c l_{c1}) \cos(k_c l_{c2})}{\sin(k_c l_{c1} + k_c l_{c2})}. \tag{13}$$

Furthermore, in accordance with the impedance transfer relationship [36,41], the acoustic impedance Z_4 at cross-section 4 is determined as

$$Z_4 = Z_n \frac{Z_c + iZ_n \tan(k_n l_n)}{Z_n + iZ_c \tan(k_n l_n)}, \tag{14}$$

where the term $\tan(k_n l_n)$ equals zero when the length l_n of the coupling aperture in region III is designed to be less than one wavelength and, consequently, $Z_4 \approx Z_c$.

According to Eq. (5),

$$\frac{(P_1 - P_2) Y_t}{P_3 + P_4} = \frac{(P_3 - P_4) Y_t}{P_3 + P_4} + \frac{2(P_5 - P_6) Y_n}{P_5 + P_6}, \tag{15}$$

where $P_5 + P_6/(P_5 - P_6) Y_n = Z_4$ denotes the acoustic impendence of region III at cross-section 4 in Fig. 1(c). Then, combining $P_1 + P_2 = P_3 + P_4$ with Eqs. (7) and (8) generates

$$\left(2P_t C e^{-ik_t l_2} - \frac{8P_i - 2P_t (D e^{ik_t l_2} + C e^{-ik_t l_2}) B e^{ik_t l_1}}{A e^{-ik_t l_1} - B e^{ik_t l_1}}\right) = \frac{1}{(Z_4/2) Y_t} P_t (D e^{ik_t l_2} + C e^{-ik_t l_2}). \tag{16}$$

Hence, the pressure transmission coefficient (defined as $T_P = |P_t/P_i|$) of the proposed metasurface can be derived as

$$T_P = \frac{8 \left| \frac{Z_4}{2} Y_t \right|}{|M - N|}, \tag{17}$$

where $M = 2(Z_4/2) Y_t \{B[C + D e^{2ik_t l_2}] e^{ik_t (l_1 - l_2)}\}$ and $N = \{[A - B e^{2ik_t l_1}] e^{-ik_t (l_1 + l_2)} [C + D e^{2ik_t l_2} - 2C (Z_4/2) Y_t]\}$.

When waves propagate from one medium (Z_i) to another medium (Z_{trans}), the energy transmission coefficient T_E is determined as

$$T_E = T_P^2 \frac{Z_i}{Z_{\text{trans}}}. \tag{18}$$

Equations (17) and (18) reveal that the energy transmission coefficient T_E of the heterogeneous interface depends on the geometric parameters of the microstructure and the impedance ratio of the incident and transmitted media, while the pressure transmission coefficient T_P is only determined by the geometric parameters. This means that intricately adjusting parameters can make T_P equal to $\sqrt{Z_{\text{trans}}/Z_i}$, which can produce highly efficient acoustic energy transmission with $T_E = 1$ at the mismatching interface.

C. Theoretical analysis of acoustic energy transmission

Considering acoustic waves are incident from the air domain to a water one, the impedance $Z_t = Z_{\text{air}}$ within the microstructure is far less than the impedance $Z_{\text{trans}} = Z_{\text{water}}$ of the transmitted region and it signifies that Z_t/Z_{trans} approximates to 0, which results in $C \approx 1$ and $D \approx 1$. Thus, the terms M and N are simplified implicitly as $M = 4(Z_4/2) Y_t B e^{ik_t l_1} \cos(k_t l_2)$ and $N = \{[A - B e^{2ik_t l_1}] e^{-ik_t (l_1 + l_2)} [1 + e^{2ik_t l_2} - 2(Z_4/2) Y_t]\}$. Since there is a significant impedance difference between air and water and Z_{trans}/Z_i tends to infinity, thus, only if the pressure transmission coefficient T_P tends to infinity can $T_E = 1$ be accomplished as required. According to Eq. (17), $|M - N| = \left| \frac{Z_4}{2} Y_t [4B e^{ik_t l_1} \cos(k_t l_2) - 2(A - B e^{2ik_t l_1}) e^{-ik_t (l_1 + l_2)}] - (A - B e^{2ik_t l_1}) e^{-ik_t (l_1 + l_2)} (1 + e^{2ik_t l_2}) \right| \to 0$ and $Z_4 \neq 0$ need to be satisfied. That is to say, the above equalities hold when $(Z_4/2) Y_t = \Psi$ and $Z_4 \neq 0$, in which

$$\Psi = \frac{(A - B e^{2ik_t l_1}) e^{-ik_t (l_1 + l_2)} (1 + e^{2ik_t l_2})}{4B e^{ik_t l_1} \cos(k_t l_2) + 2(A - B e^{2ik_t l_1}) e^{-ik_t (l_1 + l_2)}}.$$

The left-hand side term $(Z_4/2) Y_t$ is determined by the coupling apertures when the channel is fixed.

For symmetrical configuration SC-1 (its detailed dimensions are given in Table I), the acoustic impedance features are analyzed and presented in Fig. 2(a). Here, $Z_4 Y_t/2$ and Ψ exhibit diverse trends and periodicity in the frequency domain and are closely interrelated with the resonant states in the coupling apertures and the channel. The imaginary component of $Z_4 Y_t/2$ possesses periodical variation characteristics and mutation points, while the real component is constantly at zero. Between the two contiguous resonance points, the imaginary component increases monotonically from negative to positive values. Furthermore, the real component of Ψ is also almost equal to zero except for the resonant points.

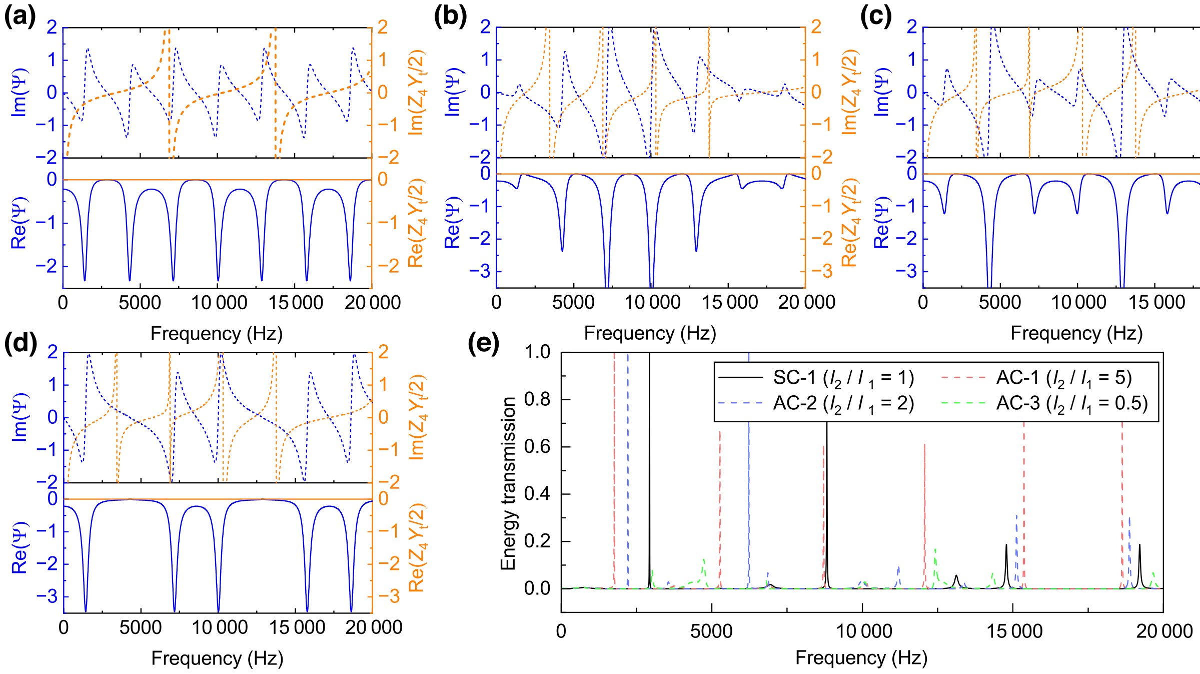

FIG. 2. Theoretical impedance spectrum and acoustic energy transmission spectrum of the designed air-water metasurface. Spectrum analysis of $Z_4Y_t/2$ and Ψ for the microstructures with different geometric symmetry: (a) configuration SC-1 with $l_2/l_1 = 1$, (b) configuration AS-1 with $l_2/l_1 = 5$, (c) configuration AS-2 with $l_2/l_1 = 2$, and (d) configuration AS-3 with $l_2/l_1 = 0.5$, where their detailed geometric parameters are given in Table I. (e) Theoretical energy transmission spectrum of the microstructures.

According to the variation of $Z_4Y_t/2$ and Ψ in Fig. 2, it can be revealed that the real components on both sides of $Z_4Y_t/2 = \Psi$ are equal (approximately) to zero at the frequencies distant from the resonance points. Consequently, if the nonzero imaginary components are designed to be consistent, $Z_4Y_t/2 = \Psi$ and $Z_4 \neq 0$ are both satisfied, which implies that highly efficient acoustic energy transmission across the air-water interface can be implemented via the proposed impedance-modulating metasurface. To validate this, the theoretical transmission coefficients are calculated, see Fig. 2(e). There are two energy transmission peaks at 2966.5 Hz and 8924.3 Hz with a frequency range of 0–10 kHz. In Table II, at the first peak, the real component of Ψ is extremely small and approximate to that of $Z_4Y_t/2$, when their nonzero imaginary components are equal. Similarly, at the second peak, the real components are zero and nonzero imaginary components are also equal. Thus, it is proved that, after obtaining the zero real components, adjusting the frequency to make the nonzero imaginary components equal can produce highly efficient energy transmission through the air-water interface.

TABLE I. Geometric parameters of the symmetric and asymmetric configurations for the proposed microstructure.

Parameters	Symmetric configuration	Asymmetric configuration		
	SC-1	AC-1	AC-2	AC-3
h_{unit}	23.0 mm	23.0 mm	23.0 mm	23.0 mm
l_1	30.0 mm	10.0 mm	20 mm	40.0 mm
l_2	30.0 mm	50.0 mm	40 mm	20.0 mm
l_2/l_1	1	5	2	0.5
h_{t}	5.0 mm	5.0 mm	5.0 mm	5.0 mm
l_{c1}	25.0 mm	5.0 mm	15.0 mm	35.0 mm
l_{c2}	25.0 mm	45.0 mm	35.0 mm	15.0 mm
h_{c}	5.0 mm	5.0 mm	5.0 mm	5.0 mm
l_{n}	1.5 mm	1.5 mm	1.5 mm	1.5 mm
h_{n}	5.0 mm	5.0 mm	5.0 mm	5.0 mm

The term $Z_4Y_t/2$ is primarily defined by the geometrical parameters l_{c1} and l_{c2} of the resonators, while the term Ψ only depends on the parameters l_1 and l_2 due to the fixed h_t and h_{unit}. Under the given restriction of $l_1 - l_{c1} = l_2 - l_{c2}$, the microstructure symmetry is customized by regulating the position of the coupling apertures. To investigate the influence of

TABLE II. Impedance analysis of the configuration SC-1 at the energy transmission peaks.

Peak	Real (Ψ)	Imag. (Ψ)	Real ($Z_4Y_t/2$)	Imag. ($Z_4Y_t/2$)
2966.5 Hz	-6.5×10^{-4}	−0.0549	0	−0.0549
8924.3 Hz	-7.7×10^{-3}	−0.1850	0	−0.1851

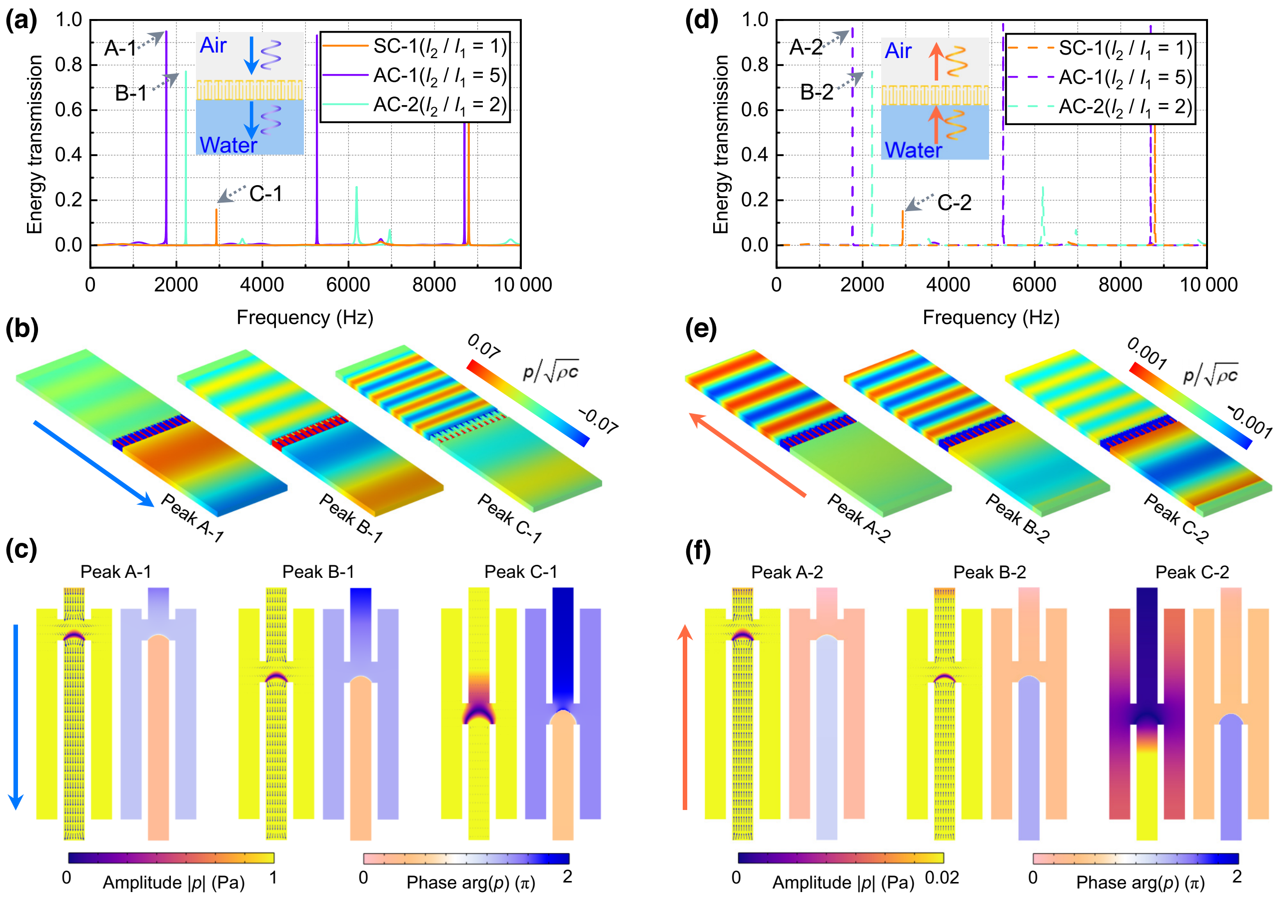

FIG. 3. Numerical simulation characterization of the proposed metasurface. (a) Simulated acoustic energy transmission of the incident waves from the air-to-water domains for three different configurations, i.e., SC-1, AC-1, and AC-2. (b) Simulated acoustic pressure fields determined as $p/\sqrt{\rho c}$ for the marked peaks, A-1, B-1, and C-1, in (a). (c) Pressure amplitude $|p|$ and phase $\arg(p)$ fields of the microstructures in (b). (d) Simulated acoustic energy transmission of the incident waves from the water-to-air domains for three different configurations, i.e., SC-1, AC-1, and AC-2. (e) Simulated acoustic pressure fields determined as $p/\sqrt{\rho c}$ for the marked peaks, A-2, B-2, and C-2, in (d). (f) Pressure amplitude $|p|$ and phase $\arg(p)$ fields of the microstructures in (e).

microstructure symmetry on the theoretically enhancing transmission behavior, an impedance characteristic analysis of three different asymmetric configurations, i.e., AC-1, AC-2, and AC-3, is undertaken, as given in Figs. 2(b)–2(d). Compared with the symmetrical microstructure with $l_1 = l_2$, the imaginary components of $Z_4Y_t/2$ for the asymmetric microstructures with $l_1 \neq l_2$ possess more mutation points in the same frequency band. For $l_{c1} = l_{c2}$, Z_4 is correlated to $1/\tan(k_cl_{c1})$ and the imaginary component of $Z_4Y_t/2$ varies abruptly under $k_cl_{c1} + k_cl_{c2} = 2m\pi\,(m = 1, 2, 3, \ldots)$. For $l_{c1} \neq l_{c2}$, Z_4 is correlated to $1/[\tan(k_cl_{c1}) + \tan(k_cl_{c2})]$ and the condition $k_cl_{c1} + k_cl_{c2} = m\pi\,(m = 1, 2, 3, \ldots)$ triggers the abrupt variation. The $Z_4Y_t/2$ spectrum curves of the asymmetric configuration possess a smaller mutation period and its resonance points number is twice as many as the of the symmetric configuration in the same band. When the spectrum curves of the microstructures AS-2 and AS-3 are completely consistent, the microstructure AS-1 has the same resonance points but slightly different variation trends at nonresonance points. In the Ψ spectrum of the asymmetric design, there are still several resonance points, although the curves are greatly different from those of the symmetric design. The real components are almost equal to zero except for the resonant points and nearby frequency points when the imaginary components decrease monotonically from positive to negative values within the contiguous resonance states, which is opposite to the increasing tendency of $Z_4Y_t/2$. More resonance points signify that $Z_4Y_t/2 = \Psi$ and $Z_4 \neq 0$ are satisfied more easily in the asymmetric configurations and more high energy transmission peaks arise for the mismatching interface. In Fig. 2(e), it can be found that the configuration AC-1 possesses three energy transmission

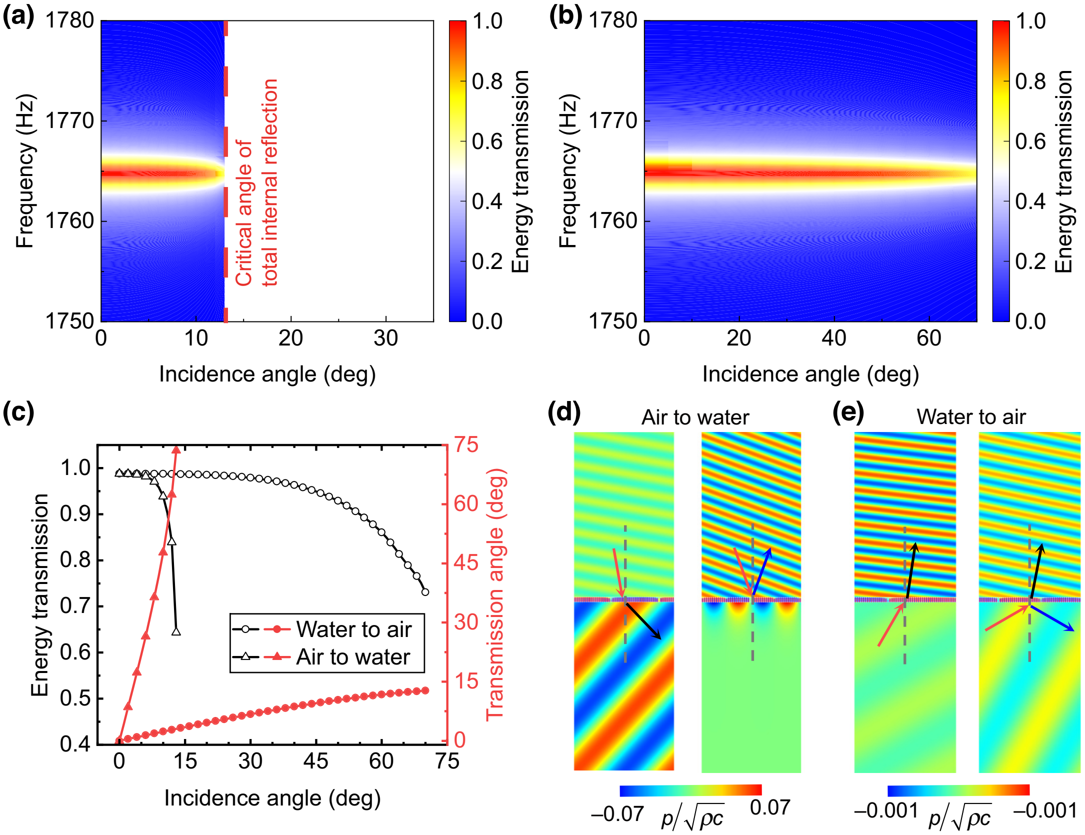

FIG. 4. Simulated transmission behavior of the oblique incidence for the configurations AC-1. The simulated frequency spectrum of the acoustic energy transmission for the oblique incidence (a) from the air-to-water domains and (b) from the water-to-air domains. (c) Energy transmission and transmission angle of the different incidence angles at the peak frequency (1765 Hz). (d) Scattering field of the air-to-water waves with the incidence angle of 10° (left) and 20° (right) at the peak frequency (1765 Hz). (e) Scattering field of the water-to-air waves with the incidence angle of 30° (left) and 40° (right) at the peak frequency (1765 Hz).

peaks within the frequency band of 1–10 kHz, which is more than the symmetric configuration SC-1. In addition, the results of the configurations AC-2 and AC-3 indicate that it is easier to produce highly efficient energy transmission when the coupling apertures are closer to the air side, i.e., $l_1 < l_2$.

III. WAVE BEHAVIOR VALIDATION VIA NUMERICAL SIMULATION AND EXPERIMENT

A. Numerical simulation characterization

To characterize the enhancing transmittance behavior of the metasurface, a finite element method was used to check the energy transmission spectrum, as displayed in Fig. 3. The numerical simulation characterization is performed by the commercial finite element software COMSOL Multiphysics. Due to the impedance mismatching between the structure and background medium, acoustic hard boundary conditions are adopted to model the metamaterials and a frequency-domain analysis is executed in the pressure acoustic module, neglecting the deviations induced by thermal viscous losses. In the simulation modeling, background pressure fields are adopted to simulate ideal incident waves when perfect matching layers are introduced to eliminate the interference of the reflective waves on the response sound fields. What needs illustration is that the simulations proceed on a single 2D unit cell constrained by Floquet-Bloch periodic boundary conditions. In addition, periodic extension and 3D stretching operations of acoustic field information are carried out during the postprocessing. Checking the cross-section-averaged sound pressure in the transmitted domain, the acoustic energy transmission coefficients are subsequently determined. The material parameters of the water medium are given as mass density $\rho_{\text{water}} = 998$ kg/m^3 and acoustic velocity $c_{\text{water}} = 1450$ m/s, when the material parameters of the air medium are $\rho_{\text{air}} = 1.21$ kg/m^3 and $c_{\text{air}} = 343$ m/s.

When acoustic waves are incident from the air-to-water domains, multiple transmission peaks appear within the frequency band of 0–10 kHz, as shown in Fig. 3(a), which coincides fairly effectively with the theoretical results (Fig. 2). For the highly asymmetric configuration AC-1, the three peak frequencies are 1765, 5267 and 8695 Hz

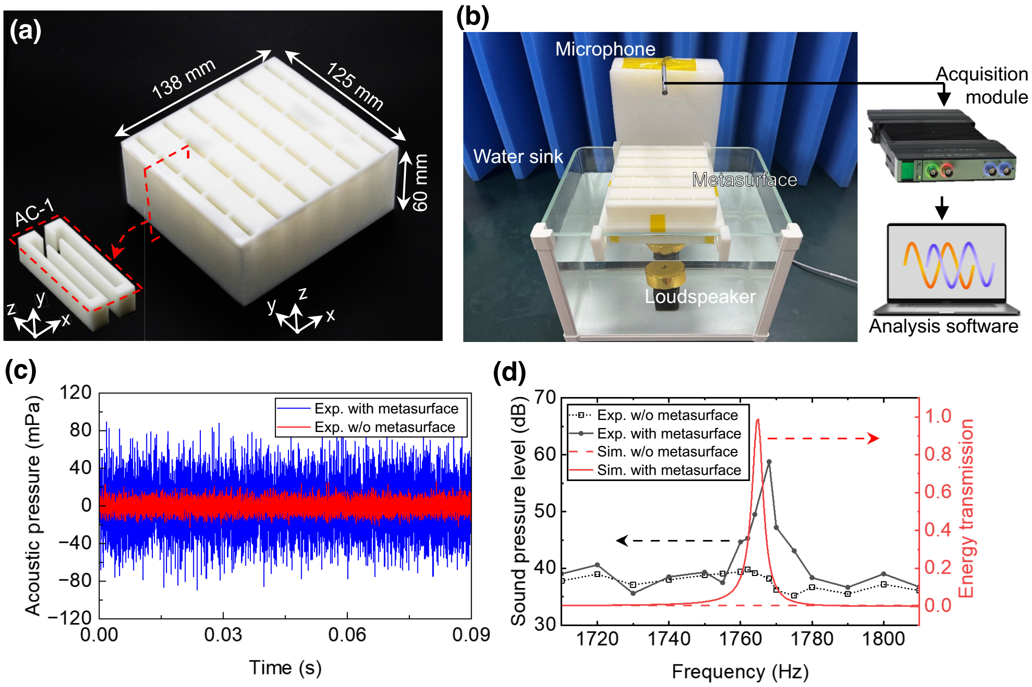

FIG. 5. Experimental characterization of acoustic transmittance behavior across the air-water interface. (a) Photograph of the manufactured air-water metasurface sample with the configuration AC-1. (b) Photograph of the experimental platform. (c) Experimental time-domain signals with and without the metasurface sample when the incident wave is set to a frequency of 1768 Hz. (d) Experimental sound pressure level in the air domain and numerically simulated energy transmission, where the black solid and dashed lines denote the experimental response spectrum with and without the metasurface sample, respectively, and red lines signify the simulated transmission spectrums.

(1763, 5270 and 8710 Hz from theory). Configuration AC-2 has two obvious peaks (>0.2) at 2219 and 6185 Hz (2215 and 6230 Hz from theory). Configuration SC-1 has two obvious peaks at 2931 and 8794 Hz (2930 and 8820 Hz from theory). Different from the initial peaks, which have a fair consistency, the simulated results deviate from the theoretical analysis for other peaks in the higher frequency range, which is caused by the high-order diffraction modes being nonnegligible at high frequencies (not considered in the theory). For the initial peaks, the asymmetric design with larger l_2/l_1 contributes to enhancing the air-water energy transmission at lower frequencies. In Fig. 3(b), at peak A-1, acoustic waves incident from the air domain can transmit into the water domain without any palpable reflection at the interface. Although a little incident energy is blocked at peak B-1, most energy can pass through the air-water interface. In contrast, the transmitted component is less than the reflected component of incident acoustic energy at peak C-1 of the configuration SC-1. To analyze the wave mechanism of the metasurface, Fig. 3(c) presents the pressure amplitude $|p|$ and phase $\arg(p)$ fields of the microstructures at peaks A-1, B-1, and C-1. At the junctions of the long channels and the coupling apertures, there are obvious zero-pressure zones accompanied by a phase mutation of π. For peaks A-1 and B-1, acoustic energy propagating forward can break through the zero-pressure zones. However, the large zero-pressure zone in the configuration AC-2 at peak C-1 allows only a small amount of energy to pass through, which results in a lower transmission efficiency [see Fig. 3(a)] compared with peaks A-1 and B-1.

To investigate the reciprocal propagation of the metasurface, the energy transmission enhancement behavior for water-to-air waves is simulated in Fig. 3(d). The transmission spectrum of the incident waves from the water domain is completely consistent with that of the waves from the air domain. At peak A-2, the metasurface supports the perfect acoustic energy transmission across the mismatching interface, as shown in Fig. 3(e). At peak B-2, the metasurface consisting of the configuration AC-2 can help most incident energy from the water domain continue propagating forward despite blocking a little incident energy. In addition, the symmetric metasurface can also enhance energy transmission at peak C-2, notwithstanding the blocked majority. The metasurface with dual coupling resonators possesses the extraordinary capabilities of bidirectional energy transmission enhancement at the air-water interface. Furthermore, as shown in Fig. 3(f), the acoustic response fields of the peaks A-2, B-2, and C-2 exhibit similar phenomena to those of peaks A-1, B-1, and C-1.

To investigate the influence of oblique incidence on the cross-media transmission behavior, the transmission spectrums of the different incidence angles are given in Figs. 4(a) and 4(b) for the configuration AC-1. The proposed metasurface at the air-water interface obeys Snell's law. Here, increasing the incidence angle would not shift the peak frequencies of the energy transmission. For the air-to-water oblique incidence, the refraction angle is much larger than the incidence angle owing to the acoustic velocity difference between water and air, as displayed in Fig. 4(c). The peak efficiency is maintained above 0.9 within an angle range of 0°–10°, while increasing the angle results in the significant deterioration of the transmission efficiency. Moreover, there is a critical angle of total internal reflection, $\theta_{ic} = \arcsin(c_{\text{air}}/c_{\text{water}}) \approx 13.28^\circ$, as shown in Fig. 4(a). When the incident angle is larger than θ_{ic}, the incident acoustic energy is completely reflected. As shown in the right-hand side image of Fig. 4(d), the incident wave with the angle of 20° and the frequency of 1765 Hz at the air domain is fully reflected at the interface, while only near-field diffraction modes exist, which is different from the scattering field of 20° (the left-hand side image). For the water-to-air oblique incidence, although the critical angle θ_{ic} is nonexistent theoretically, energy transmission efficiency through the heterogeneous interface decreases at wide angles [in Fig. 4(c)]. The water-to-air transmission efficiency of the 70° incident angle is 0.73. The proposed metasurface (consisting of configuration AC-1), however, has robust and highly efficient (>0.9) water-to-air transmission features within the wide-angle range of 0°–55°. For example, the reflected component is quite weak in the scattering field of the 30° incident angle, as shown in Fig. 4(e), when the reflected component of the 60° incident angle is relatively more clearly seen and the transmission efficiency is 0.86.

B. Experimental characterization

To qualitatively characterize the acoustic energy transmission, Fig. 5 portrays a platform composed of an air-water acoustic environment, a metasurface sample, and an acoustic measurement system. The metasurface sample is constructed by a 6×5 array arrangement of the microstructural element, as given in Fig. 5(a), while the element is formed by stretched configuration AC-1 (with a thickness of 23 mm) and two baffle plates (with a thickness of 1 mm) on both sides. The metasurface specimen is manufactured using 3D printing technology provided by WeNext Technology Co., Ltd. and WeNext 8000-type light-cured resin is selected as the base material. The machining accuracy is 0.1 mm so that the design dimensions of the metasurface can be satisfied.

To construct the acoustic environment of the experimental platform, as displayed in Fig. 5(b), a waterproof loudspeaker as an acoustic source is prepared and placed into water within a water sink. The loudspeaker can be remotely controlled by conventional Bluetooth technology to emit acoustic waves with preset frequencies. To reduce the vibration of the setup caused by the loudspeaker and suppress the outward radiation of acoustic energy, the water sink and the loudspeaker are positioned onto an acoustic sponge. Furthermore, the acoustic sponge is also arranged around the experimental setup to reduce the interference of the reflected acoustic field in air. The acoustic measurement system is constructed by Brüel & Kjær test instruments, which consist of a signal acquisition module (type 3160-A-042), a microphone (type 4138-A-015) with a diameter of 1/8-inch, a self-contained acoustic signal analysis software, and several self-contained connecting wirings.

When the loudspeaker emits sound waves at preset frequencies, the microphone positioned above the water accurately senses the transmitted acoustic signals across the air-water interface, and the acquisition module captures the time-domain signals. As shown in Fig. 5(c), when the incident wave is set to a frequency of 1768 Hz, only extremely weak acoustic signals are sensed on the bare interface, but the metasurface sample significantly helps the microphone capture stronger signals. The response spectrum of the sound pressure level is obtained by performing Fourier transform processing on the time-domain signals. In Fig. 5(d), the apparent difference between the black solid and dashed lines illustrates that the sample possesses the capability of enhancing acoustic energy transmission across the air-water interface within the designed band. For an incident wave from the water domain set at 1768 Hz, the measured sound pressure level in the air domain is approximately 58 dB under the assistance of the metasurface sample, and it decreases to 39 dB after removing the metasurface sample.

IV. WIRELESS ENERGY HARVESTING VIA METASURFACE AND TENG

A. Integrated adoption of TENG

To implement the functionality of acoustic energy transmission and harvesting across the air-water interface, triboelectric nanogenerators [42–44] are introduced to convert acoustic energy to electrical energy. Triboelectric nanogenerators, driven by the acoustic waves, can produce high output voltage [42–45]. They are flexible multilayer film structures with a lower stiffness and lower acoustic impedance, which facilitates airborne sound energy to enter them. In Fig. 6(a), a structural TENG is proposed based on the physical mechanism of vertical contact-separation mode [45,46], and it consists of a polytetrafluoroethylene (PTFE) film as the middle layer and two copper (Cu) films as electrodes at the lower and upper layers. Different from the upper electrode adhered to the PTFE

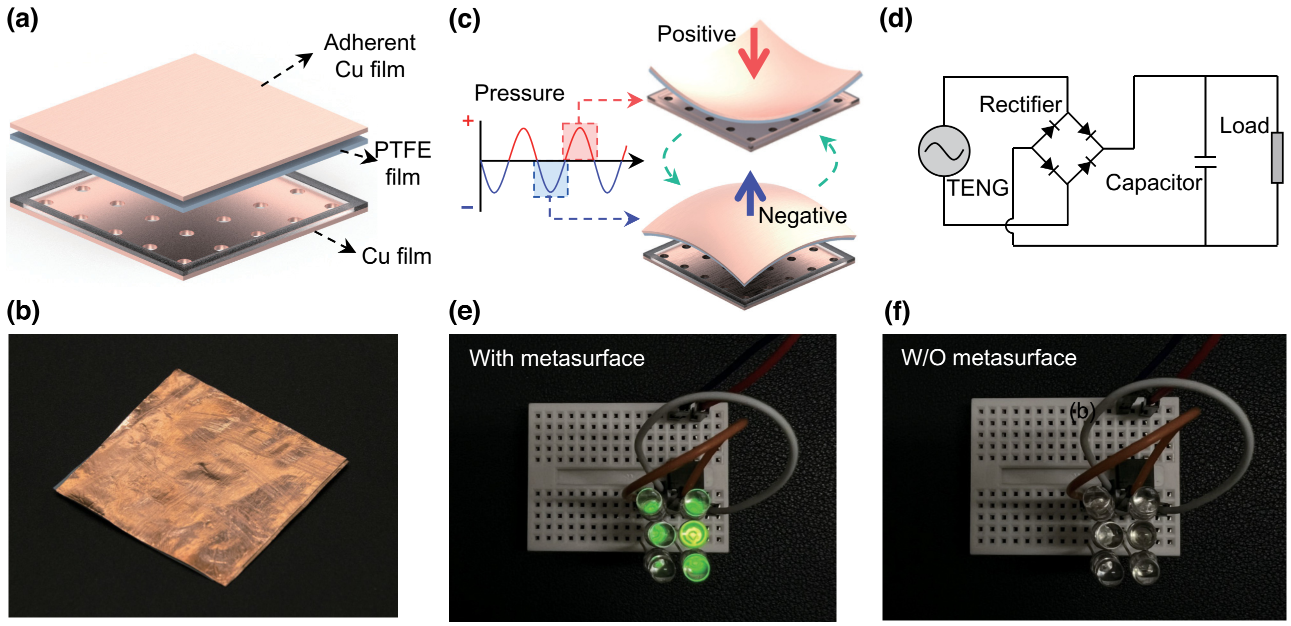

FIG. 6. Wireless acoustic energy harvesting via AWM-TENG devices across the air-water interface. (a) Design of the structural TENG based on a vertical contact-separation mode mechanism. The dimensions of PTFE film are 50 mm × 50 mm × 0.05 mm. The dimensions of Cu films are 50 mm × 50 mm × 0.05 mm. (b) Photograph of prepared structural TENG sample used in the experiments. (c) Oscillating motion schematic of the PTFE film in the acoustic pressure field. (d) Circuit diagram with a full-bridge rectifier used in the energy harvesting experiments. LED lamps driven by the TENG (e) with and (f) without the proposed air-water metasurface sample.

film, the lower electrode is designed with holes. Contacting with the lower Cu electrode, the PTFE generates a bulk charge transfer owing to its strong electronegativity [46,47]. Acoustic waves propagating in the medium can cause the deformation and vibration of the flexible film. In the acoustic field, the periodic variation of the wave front pressure can arouse the repeat oscillating motion of the PTFE film, as shown in Fig. 6(c). The radiation force of the positive pressure field induces the PTFE film to deform and approach the lower Cu electrode. However, the negative pressure can generate the separation between the PTFE film and the lower electrode. Thus, the harmonic acoustic field can produce the periodic contact-separation motion in the structural TENG. A detailed explanation of the acoustic-electric energy conversion mechanism is given in Appendix A.

B. Experimental implementation of cross-media energy harvesting

To realize the wireless harvesting of acoustic energy across the air-water interface, the structural TENG device is manufactured, as depicted in Fig. 6(b), and positioned above the metasurface sample. After enhancing the energy transmission at the air-water interface through the metasurface, the structural TENG converts acoustic energy from the water domain to electrical energy for harvesting and powering external electronic devices. Considering that the power delivered from the TENG device is an alternating current, a full-bridge rectifier is adopted to capture the energy, as shown in Fig. 6(d). In Figs. 6(e)–6(f), with the collaborative assistance of the metasurface sample and the TENG devices, the underwater acoustic energy at 1768 Hz is delivered and can continuously light six LED lamps with about 0.1 W in the air domain. Conversely, the lamps are turned off once the proposed metasurface sample is removed. Benefiting from the metasurface-TENG integrated system, underwater acoustic energy can be transmitted remotely and harvested wirelessly across the air-water interface.

V. CONCLUSION

In summary, this work proposed an air-water metasurface with dual coupling resonators for wireless transmission and the harvesting of acoustic energy across the air-water interface. After presenting the theory of acoustic energy transmission, wave propagation behavior in the designed metasurface was analyzed to clarify theoretical design conditions and the physical mechanism of high transmission. Then, the enhancement of bidirectional acoustic energy transmission of the proposed metasurface with symmetrical and asymmetrical microstructures was investigated and verified numerically. Qualitative experiments further indicated the elaborately designed metasurface can effectively improve energy transmission at the heterogeneous interface. Finally, integrating the designed metasurface and a structural triboelectric nanogenerator realized wireless acoustic energy harvesting across the air-water interface, which successfully operates six LED lamps with about 0.1 W. Our methodology opens the way for remote wireless energy-supplying technology across the air-water interface for electronic equipment such as autonomous underwater vehicles, underwater passive sensors, and deep-sea observation networks.

The data that support the findings of this study are available from the corresponding author upon reasonable request.

ACKNOWLEDGMENTS

This work was supported by the National Natural Science Foundation of China (Grants No. 52250217 and 12172044, the Beijing Institute of Technology Research Fund Program for Young Scholars, and the Postdoctoral Fellowship Program of China Postdoctoral Science Foundation (Grant No. GZC20242179).

Z. Ren: conceptualization, methodology, formal analysis, visualization, and writing—original draft. H.-W. Dong: conceptualization, data curation, funding acquisition, writing—review & editing, and project administration. S.-D. Zhao: validation and discussion. M. Chen: discussion and writing—review & editing. D. Fang: supervision, writing—review & editing, and project administration.

The authors declare that they have no known competing financial interests or personal relationships that could have appeared to influence the work reported in this paper.

APPENDIX A: ACOUSTIC-ELECTRIC ENERGY CONVERSION MECHANISM OF THE STRUCTURAL TENG

To clearly explain the acoustic-electric energy conversion mechanism of the structural TENG, a schematic diagram of free electron transportation is shown in Fig. 7(b). Furthermore, the motion of the PTFE film in the TENG in the acoustic pressure field in a single conversion cycle and the resulting spatial potential variation of the TENG are given in Fig. 7(a). In order to exhibit the fairly spatial electrostatic potential caused by triboelectric charges, the numerical simulation of the potential distribution is carried out on a 2D TENG model under open-circuit conditions, as shown in Fig. 7(c). In a single oscillating motion, the PTFE film contacts with the Cu film at the initial stage (stage s-i), and then the resulting coincident electron clouds on the films' surfaces cause free electrons from the lower electrode to enter the deeper potential well of the PTFE film [48]. The contacting mode induces zero spatial potential (stage p-i), although the PTFE has a negative charge opposite to the lower Cu electrode after free electron transportation. When the PTFE film and the Cu film are separated by the acoustic pressure field, the negative and positive charges in the films no longer coincide on the

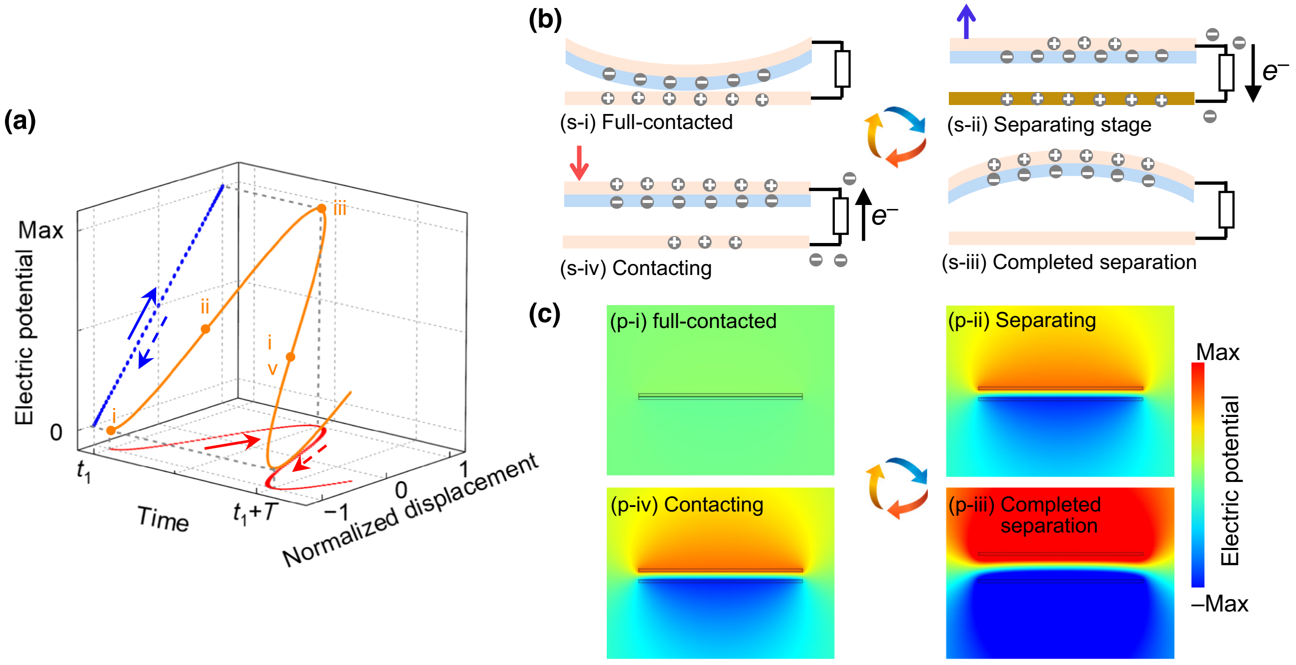

FIG. 7. Acoustic-electric energy conversion mechanism of the structural TENG. (a) Motion of the PTFE film and spatial potential variation of the TENG in a single conversion cycle. (b) Free electron transportation in the TENG at different stages (s-i, ss-ii, s-iii, and s-iv) during the acoustic-electric energy conversion. (c) Simulated spatial potential distribution in the TENG at different stages (p-i, p-ii, p-iii, and p-iv). These four stages correspond to four marked points in (a).

same plane, which leads to an inner dipole moment and an increased nonzero electric potential field between the films (stage p-ii). To screen the local electric field, the electrons in the upper Cu film are driven and flow to the lower Cu electrode through the external circuit load (stage s-ii) until the maximum separation (stage s-iii). Subsequently, the PTFE film approaches the lower Cu electrode, and the reduced separation weakens the spatial potential difference (stage p-iv), which drives the free electrons transportation from the lower electrode to the upper one through the external circuit load (stage s-iv). A full period of acoustic-electric energy conversion ends with the recontact of the films, and the charge and potential distribution return to the initial state. Then, acquiring the momentum from the acoustic waves, the PTFE film bounces off the Cu films and the structural TENG enters another conversion cycle.

[1] E. Dong, P. Cao, J. Zhang, S. Zhang, N. X. Fang, and Y. Zhang, Underwater acoustic metamaterials, Natl. Sci. Rev. **10**, nwac246 (2023).

[2] H.-W. Dong, S.-D. Zhao, X.-B. Miao, C. Shen, X. Zhang, Z. Zhao, C. Zhang, Y.-S. Wang, and L. Cheng, Customized broadband pentamode metamaterials by topology optimization, J. Mech. Phys. Solids **152**, 104407 (2021).

[3] G. S. Shekhawat, S. M. Dudek, and V. P. Dravid, Development of ultrasound bioprobe for biological imaging, Sci. Adv. **3**, e1701176 (2017).

[4] R. W. Bourdeau, A. Lee-Gosselin, A. Lakshmanan, A. Farhadi, S. R. Kumar, S. P. Nety, and M. G. Shapiro, Acoustic reporter genes for noninvasive imaging of microorganisms in mammalian hosts, Nature **553**, 86 (2018).

[5] C. Ma, S. Kim, and N. X. Fang, Far-field acoustic subwavelength imaging and edge detection based on spatial filtering and wave vector conversion, Nat. Commun. **10**, 204 (2019).

[6] M. J. Buckingham, E. M. Giddens, F. Simonet, and T. R. Hahn, Propeller noise from a light aircraft for low-frequency measurements of the speed of sound in a marine sediment, J. Comput. Acoust. **10**, 445 (2002).

[7] Y. Liu, D. Habibi, D. Chai, X. M. Wang, H. Chen, Y. Gao, and S. Y. Li, A comprehensive review of acoustic methods for locating underground pipelines, Appl. Sci. **10**, 1031 (2020).

[8] R. Williams, C. Erbe, A. Duncan, K. Nielsen, T. Washburn, and C. Smith, Noise from deep-sea mining may span vast ocean areas, Science **377**, 157 (2022).

[9] E. Dong, Y. Zhang, Z. Song, T. Zhang, C. Cai, and N. X. Fang, Physical modeling and validation of porpoises' directional emission via hybrid metamaterials, Natl. Sci. Rev. **6**, 921 (2019).

[10] F. Y. Yang, P. M. Lee, Z. Y. Dong, X. Tian, and J. S. Ho, Enhancing wireless transmission from the body with wearable diffractive patterns, Phys. Rev. Appl. **12**, 054020 (2019).

[11] X. D. Meng, R. X. Liu, H. C. Chu, R. W. Peng, M. Wang, Y. Hao, and Y. Lai, Through-wall wireless communication enabled by a metalens, Phys. Rev. Appl. **17**, 064027 (2022).

[12] B. Assouar, B. Liang, Y. Wu, Y. Li, J. C. Cheng, and Y. Jing, Acoustic metasurfaces, Nat. Rev. Mater. **3**, 460 (2018).

[13] Y. F. Zhu and B. Assouar, Multifunctional acoustic metasurface based on an array of Helmholtz resonators, Phys. Rev. B **99**, 174109 (2019).

[14] Y. F. Zhu, L. Y. Cao, A. Merkel, S. W. Fan, B. Vincent, and B. Assouar, Janus acoustic metascreen with nonreciprocal and reconfigurable phase modulations, Nat. Commun. **12**, 7089 (2021).

[15] H.-W. Dong, S.-D. Zhao, P. Xiang, B. Wang, C. Zhang, L. Cheng, Y.-S. Wang, and D. Fang, Porous-solid metaconverters for broadband underwater sound absorption and insulation, Phys. Rev. Appl. **19**, 044074 (2023).

[16] C. Shen, C. Rohde, C. W. Cushing, J. F. Li, Z. J. Tan, H. F. Du, X. Y. Peng, P. S. Wilson, M. R. Haberman, N. X. Fang, and S. A. Cummer, Anisotropic metallic microlattice structures for underwater operations, Adv. Eng. Mater. **25**, 202201294 (2023).

[17] H.-W. Dong, S.-D. Zhao, Y.-S. Wang, and C. Zhang, Topology optimization of anisotropic broadband double-negative elastic metamaterials, J. Mech. Phys. Solids **105**, 54 (2017).

[18] H.-W. Dong, C. Shen, S.-D. Zhao, W. Qiu, H. Zheng, C. Zhang, S. A. Cummer, Y.-S. Wang, D. Fang, and L. Cheng, Achromatic metasurfaces by dispersion customization for ultra-broadband acoustic beam engineering, Natl. Sci. Rev. **9**, nwac030 (2022).

[19] C. Il Park, C. Piao, H. Lee, and Y. Y. Kim, Elastic complementary meta-layer for ultrasound penetration through solid/liquid/gas barriers, Int. J. Mech. Sci. **206**, 106619 (2021).

[20] H.-W. Dong, S.-D. Zhao, M. Oudich, C. Shen, C. Zhang, L. Cheng, Y.-S. Wang, and D. Fang, Reflective Metasurfaces with multiple elastic mode conversions for broadband underwater sound absorption, Phys. Rev. Appl. **17**, 044013 (2022).

[21] J. Cao, H. Ma, S. Xie, J. Li, Y. Li, and Q. Cheng, Highly efficient abnormal reflection via underwater acoustic metagratings, Phys. Rev. Appl. **21**, 034015 (2024).

[22] O. A. Godin, Anomalous transparency of water-air interface for low-frequency sound, Phys. Rev. Lett. **97**, 164301 (2006).

[23] D. C. Woods, J. S. Bolton, and J. F. Rhoads, On the use of evanescent plane waves for low-frequency energy transmission across material interfaces, J. Acoust. Soc. Am. **138**, 2062 (2015).

[24] E. Bok, J. J. Park, H. Choi, C. K. Han, O. B. Wright, and S. H. Lee, Metasurface for water-to-air sound transmission, Phys. Rev. Lett. **120**, 044302 (2018).

[25] A. Bretagne, A. Tourin, and V. Leroy, Enhanced and reduced transmission of acoustic waves with bubble metascreens, Appl. Phys. Lett. **99**, 221906 (2011).

[26] T. Lee and H. Iizuka, Sound propagation across the air/water interface by a critically coupled resonant bubble, Phys. Rev. B **102**, 104105 (2020).

[27] Z. R. Cai, S. D. Zhao, Z. D. Huang, Z. Li, M. Su, Z. Y. Zhang, Z. P. Zhao, X. T. Hu, Y. S. Wang, and Y. L. Song, Bubble architectures for locally resonant acoustic metamaterials, Adv. Funct. Mater. **29**, 1906984 (2019).

[28] Z. D. Huang, S. D. Zhao, Y. Y. Zhang, Z. R. Cai, Z. Li, J. F. Xiao, M. Su, Q. Q. Guo, C. Z. Zhang, Y. Z. Pan, X. B.

Cai, Y. L. Song, and J. Yang, Tunable fluid-type metasurface for wide-angle and multifrequency water-air acoustic transmission, Research **2021**, 9757943 (2021).

[29] Z. D. Huang, Z. P. Zhao, S. D. Zhao, X. B. Cai, Y. Y. Zhang, Z. R. Cai, H. Z. Li, Z. Li, M. Su, C. Z. Zhang, Y. Z. Pan, Y. L. Song, and J. Yang, Lotus metasurface for wide-angle intermediate-frequency water-air acoustic transmission, ACS Appl. Mater. Interfaces **13**, 53242 (2021).

[30] P. Zhou, H. Jia, Y. Bi, Y. Yang, Y. Yang, P. Zhang, and J. Yang, Water–air acoustic communication based on broadband impedance matching, Appl. Phys. Lett. **123**, 191701 (2023).

[31] E. Q. Dong, Z. C. Song, Y. Zhang, S. G. Mosanenzadeh, Q. He, X. H. Zhao, and N. X. Fang, Bioinspired metagel with broadband tunable impedance matching, Sci. Adv. **6**, eabb3641 (2020).

[32] J. J. Liu, Z. W. Li, B. Liang, J. C. Cheng, and A. Alù, Remote water-to-air eavesdropping with a phase-engineered impedance matching metasurface, Adv. Mater. **35**, 2301799 (2023).

[33] H. T. Zhou, S. C. Zhang, T. Zhu, Y. Z. Tian, Y. F. Wang, and Y. S. Wang, Hybrid metasurfaces for perfect transmission and customized manipulation of sound across water-air interface, Adv. Sci. **10**, 2207181 (2023).

[34] J. Ji, H. Heo, J. Zhong, M. Oudich, and Y. Jing, Metamaterial-enabled wireless and contactless ultrasonic power transfer and data transmission through a metallic wall, Phys. Rev. Appl. **21**, 014059 (2024).

[35] H. Zhang, Z. Wei, L. Fan, J. Qu, and S.-y. Zhang, Tunable sound transmission at an impedance-mismatched fluidic interface assisted by a composite waveguide, Sci. Rep. **6**, 34688 (2016).

[36] S. Li, J. Xia, X. Yu, X. Zhang, and L. Cheng, A sonic black hole structure with perforated boundary for slow wave generation, J. Sound Vib. **559**, 117781 (2023).

[37] L. J. Fan and J. Mei, Metagratings for waterborne sound: Various functionalities enabled by an efficient inverse-design approach, Phys. Rev. Appl. **14**, 044003 (2020).

[38] Z. L. Hou, X. S. Fang, Y. Li, and B. Assouar, Highly efficient acoustic metagrating with strongly coupled surface grooves, Phys. Rev. Appl. **12**, 034021 (2019).

[39] Z. L. Hou, J. T. Liu, W. M. Kuang, Y. Y. Liu, and S. Z. Wu, Sonic crystal with open resonant cavities, Phys. Rev. E **75**, 026608 (2007).

[40] H. Q. Ni, X. S. Fang, Z. L. Hou, Y. Li, and B. Assouar, High-efficiency anomalous splitter by acoustic meta-grating, Phys. Rev. B **100**, 104104 (2019).

[41] C. Yang and L. Cheng, Sound absorption of microperforated panels inside compact acoustic enclosures, J. Sound Vib. **360**, 140 (2016).

[42] R. Hinchet, H. J. Yoon, H. Ryu, M. K. Kim, E. K. Choi, D. S. Kim, and S. W. Kim, Transcutaneous ultrasound energy harvesting using capacitive triboelectric technology, Science **365**, 491 (2019).

[43] C. Chen, Z. Wen, J. H. Shi, X. H. Jian, P. Y. Li, J. T. W. Yeow, and X. H. Sun, Micro triboelectric ultrasonic device for acoustic energy transfer and signal communication, Nat. Commun. **11**, 4143 (2020).

[44] H. F. Zhao, M. Y. Xu, M. R. Shu, J. An, W. B. Ding, X. Y. Liu, S. Y. Wang, C. Zhao, H. Y. Yu, H. Wang, C. Wang, X. P. Fu, X. X. Pan, G. M. Xie, and Z. L. Wang, Underwater wireless communication via TENG-generated Maxwell's displacement current, Nat. Commun. **13**, 3325 (2022).

[45] H. Wang, J. Cheng, Z. Z. Wang, L. H. Ji, and Z. L. Wang, Triboelectric nanogenerators for human-health care, Sci. Bull. **66**, 490 (2021).

[46] Y. Liu, B. D. Chen, W. Li, L. L. Zu, W. Tang, and Z. L. Wang, Bioinspired triboelectric soft robot driven by mechanical energy, Adv. Funct. Mater. **31**, 2104770 (2021).

[47] Y. Xi, J. Wang, Y. L. Zi, X. G. Li, C. B. Han, X. Cao, C. G. Hu, and Z. L. Wang, High efficient harvesting of underwater ultrasonic wave energy by triboelectric nanogenerator, Nano Energy **38**, 101 (2017).

[48] H. F. Zhao, X. Xiao, P. Xu, T. C. Zhao, L. G. Song, X. X. Pan, J. C. Mi, M. Y. Xu, and Z. L. Wang, Dual-tube Helmholtz resonator-based triboelectric nanogenerator for highly efficient harvesting of acoustic energy, Adv. Energy Mater. **9**, 1902824 (2019).